The roles of heat and gas in a mushy magma chamber

Yang Liao

[1]Department of Geology and Geophysics, Woods Hole Oceanographic Institution

Key Points:

- A physics-based model explores the influence of gas and heat in the a magma chamber containing crystal mush upon magma injection.
- The non-uniform distributions of gas and heat cause non-monotonic time evolution of deformation, crustal stresses, and magma transport.
- Poroelastic diffusion, viscous relaxation, and thermal equilibration lead to three time regimes in the post-injection evolution.

Corresponding author: Yang Liao, `yliao@whoi.edu`

Abstract

Crustal magmatic systems likely consist of magmatic reservoirs dominated by crystal mush. Recent studies suggest that the physical processes occurring in crystal mush could alter the response of magmatic reservoirs during volcanic unrest. Here, we present a magma chamber deformation model that incorporates two new aspects in crystal mush: heat and exsolved gas. The model is based on earlier studies by Liao et al. (2021) with additional processes including thermal-mechanical coupling, dependence of material properties on gas content, and temperature evolution following an injection of hotter magma. The post-injection time-dependent evolution of the system can be grouped into three periods, which are dominated by poroelastic diffusion (short term), viscoelastic relaxation (mid term), and thermal equilibration (long term). All three time-regimes are strongly affected by gas distribution, which alters the relative compressibility of the crystal-rich and crystal-poor regions in the chamber. The contribution of thermal evolution emerges during the mid-term evolution. The time-dependent evolution of the system highlights the intrinsic ability of a gas-bearing mushy magma chamber to generate non-monotonic time series of stresses, deformation, and magma transport.

Plain Language Summary

The processes that occur in magmatic reservoirs and their surrounding crustal rocks can modulate the triggering, duration, and style of volcanic eruptions. Although magmatic reservoirs are typically modeled as cavities filled with fluid magma, geophysical and petrological observations have long suggested that they likely contain crystal mush, an ensemble of solid crystals and fluid (gas/melt) that reside in interstitial pore spaces. Some recent studies show that a mushy magma chamber could behave differently than a fluid-filled chamber, leading to different interpretation of observations such as ground deformation. Here, we extend these studies to incorporate two new aspects that are typical for crustal magmatic systems: gas phase (in the form of disconnected gas bubbles) and nonuniform temperature. The incorporation of these two new aspects allows for more processes that can be examined quantitatively, and a more realistic depiction of crustal magmatic reservoirs. We find that when gas and heat distribute unevenly, a simple magma injection event could result in complex time-dependent changes in pressure, stress, and magma flows in the chamber.

1 Introduction and Background

Petrological and geophysical observations show that crustal magmatic reservoirs are likely 'mushy', containing regions dominated by crystal mush (Cashman et al., 2017; Jackson et al., 2018; Sparks et al., 2019). Recent studies show that crystal mush in a close-system magmatic reservoir could strongly influence its mechanical response to magmatic events such as magma injection (Gudmundsson, 2015; Liao et al., 2018, 2021). As the physical processes occurring in crystal mush are tied to the pressure, stress, and deformation of the surrounding crust, a better understanding of these processes could improve our ability to interpret surface observations during volcanic unrest. Incorporating crystal mush in volcano deformation models has been a recent practice, with a focus on a number of mechanical processes such a poroelastic diffusion, viscoelastic relaxation, and deformation of the host rocks.

Close-system magma chamber models typically assume isothermal conditions (Browning et al., 2015; Srigutomo et al., 2015; Segall, 2016). Heat and thermal gradients in the crust, however, have been shown to matter for ground deformation predictions. For example, the rheological structure induced by hotter host rock surrounding a magma chamber could lead to complex temporal evolution of crustal stresses, overpressure, and ground deformation (Segall, 2016; Head et al., 2021; Townsend, 2022). Thermal evolution of magmatic reservoirs and their surrounding crust may cause coalescence of adjacent reservoirs, as shown by Biggs and Annen (2019). The thermal structure in the crust could influence the transport of gaseous volatiles escaping magmatic reservoirs (Mittal & Richards, 2019). Over geologic timescales, the thermal contraction of a cooling magmatic reservoir has been shown to lead to long-term, observable ground subsidence seen in archeological sites (Tallarico et al., 2003). In mushy magma chambers, thermal gradients could likely be maintained for longer period of time than in fluid chambers, due to impeded magma mixing in regions with high crystallinity. The methods for studying thermal effects in crustal rocks could potentially be applied to the mushy regions in a mushy magma chamber.

Magmatic reservoirs that directly contribute to ground elevation are likely shallow, hence exsolved gas might exist prior to magma ascent, as suggested by petrological evidence (Wallace, 2001; Métrich & Wallace, 2008; Mordensky & Wallace, 2018; Lerner et al., 2021). Exsolved gas has been incorporated, to some extent, in both close-system magma chamber models and in open reservoir models, as well as in the host crust and volcanic conduits (Nishimura, 2004; Voight et al., 2010; Huppert & Woods, 2002; Edmonds & Woods, 2018; Wasser et al., 2021; Huber et al., 2011; Bachmann & Bergantz, 2006; Davis et al., 2007; Girona et al., 2015). For a mushy magma chamber, gas could exist in both crystal-poor region and/or in crystal mush. The distribution of gas in a mushy magma chamber could also be nonuniform, depending on crystallinity. Exsolved gas could increase the compressibility and the thermal expansion coefficient of gas-bearing magmas, which may lead to different response of the chamber to pressure and temperature changes.

Here, we present a model which incorporates the aspects of gas and heat in a partially mushy magma chamber. Our model incorporates thermal evolution in the chamber, thermal-mechanical coupling in the crystal mush, and an explicit account for gas content in either the crystal-poor and/or the crystal-rich regions.

2 Model set-up

2.1 Geometry, rheology and solution methods

The model set-up, assumptions, and solution methods closely follow Liao et al. (2018, 2021): the magma chamber is modeled as a spherical body embedded in an infinite domain of elastic host rock (Figure 1a). The chamber consists of a fluid core and a mush shell with uniform mush viscosity, compressibility, rigidity, porosity and permeability. Exsolved gas, in the form of suspended gas bubbles, exists in the fluid core and/or the interstitial pore space in the mush (Figure 1). Prior to the injection, the system is at a thermo-mechanical steady state. Inside the fluid core the temperature T_{in} is uniform and constant in time prior to injection; the temperature decreases away from the fluid core and reaches T_{out} at the mush-rock boundary (Figure 1 b). The injection occurs instantaneously at $t = 0$ when an additional 2vol% of hotter magma is mixed into the fluid core. At $t = 0^+$, heat exchange between the fluid core and the mush occurs. We examine the time-dependent evolution of several key quantities following the onset of thermal equilibration and injection, including tensile stress $\sigma_{\theta\theta}$ at the chamber's wall (a proxy for chamber deformation and ground elevation amplitude), core pressure P_c, the displacement at the core-mush boundary $u(r_o)$, and the amount of magma transported from the core fluid into the mush M_{leak}.

Compared to the previous studies, our current model explores two new aspects: non-isothermal condition (pre-injection thermal gradient in the mush, as well as hot injection), and the explicit account for exsolved gas (Segall, 2016; Gudmundsson, 2015; Liao et al., 2018, 2021). The thermal aspect is incorporated with a thermo-poro-viscoelastic rheology of the mush (i.e., thermal expansion/contraction upon temperature change leads to additional pressure change), and additional energy conservation equation. The aspect of exsolved gas is incorporated with explicit expressions of magma compressibility and

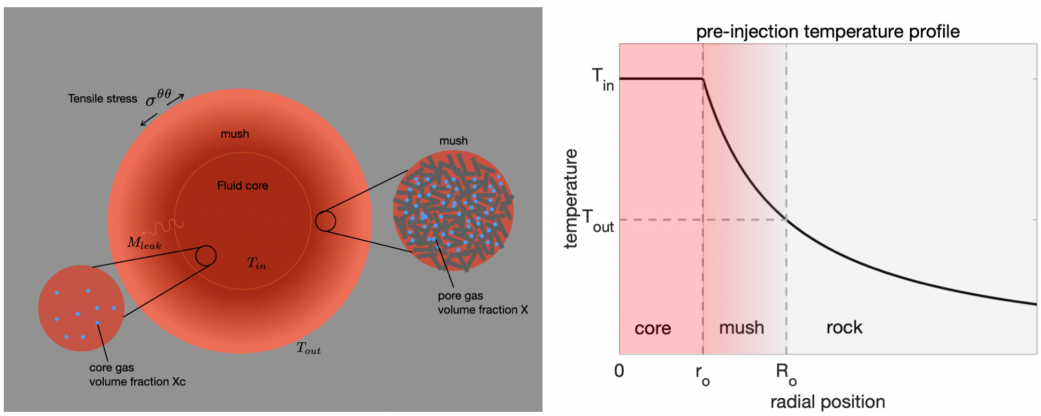

(a) (b)

Figure 1. (a) Geometry of the magma chamber model with cross-section view. The spherical magma chamber with radius R_o consists of a fluid core with radius r_o and a crystal mush shell. The zoom-in panels show the crystalline matrix with pore gas in the mush, and the gas in the core. Prior to injection the steady state temperature profile is T_{in} in the fluid core and T_{out} at the chamber's wall. Both the core magma and pore magma contain exsolved gas, with volume fraction X_c in the core and X in the pores, respectively. The tensile stress at the wall of the chamber $\sigma_{\theta\theta} = 2\frac{u(R_o)}{R_o}\mu_c$ is proportional to the deformation at the chamber's wall and the magnitude of ground deformation. (b) Steady state temperature profile prior to injection of magma. The temperature profile is a solution to the steady state thermal equilibrium $\nabla^2 T = 0$. Dash lines indicate the location of the core boundary r_o, chamber boundary R_o and definition of T_{in} and T_{out}. For the pre-injection chamber, we assume that the temperature in the fluid core T_{in} is constant in time, making the core-mush boundary r_o effectively insulating.

thermal expansion coefficient of core/pore magmas as functions of gas volume fractions. Below we describe the quantitative framework that allows us to explore these new aspects. Certain simplifications are assumed, which are discussed in the next section.

The linear thermo-poro-viscoelastic rheology assumed for mush rheology combines the classical linear poroelastic rheology, Maxwell viscoelastic relaxation model, and the equation of state of the pore fluid (Cheng, 2016). The dynamics of the system is driven by three thermal-mechanical processes: poroelastic diffusion, viscoelastic relaxation, and thermal evolution. The poroelastic diffusion process equilibrates pore pressure via porous flows; the viscoelastic relaxation process eliminates deviatoric stresses via deforming the crystalline matrix; the thermal process, largely governed by thermal diffusion, drives the system to a uniform temperature. Assuming negligible thermal contraction of solid crystals, the constitutive relations governing the deformation of the mush and the pore magma content are (Biot, 1941; Cheng, 2016; Mittal & Richards, 2019; Liao et al., 2021)

$$\dot{\sigma}_{ij} + \frac{\mu}{\eta}\sigma_{ij} = \frac{\mu}{\eta}(K_m\epsilon - \alpha P)I + 2\mu\dot{\epsilon}_{ij} + (K_m - \frac{2}{3}\mu)\dot{\epsilon}I - \alpha\dot{P}I - 3K_m\beta_s TI \tag{1a}$$

$$\zeta = \alpha\epsilon + \frac{\alpha^2}{K_u - K_m}P - \left(\phi\beta_{pore} + (\alpha-\phi)\beta_s\right)T \tag{1b}$$

where the overhead dot $\dot{}$ denotes partial derivative in time, I denotes identity matrix. σ_{ij} and ϵ_{ij} are stress and strain tensors of the ensemble material, ϵ is the volumetric strain, P is the pore pressure, T is the temperature variation from its reference value.ζ is the variation of fluid content, defined as the increment of pore fluid volume per un-deformed volume of mush. μ and η are the shear modulus and shear viscosity of the crystalline framework, α is the Biot coefficient of poroelasticity, and ϕ is the porosity in the mush. β_s is the thermal expansion coefficient for the solid crystals, which is assumed to be 0 (i.e., thermal deformation occurs only in the fluid component). The thermal expansion coefficient of the gas-rich pore magma $\beta_{pore} = (1-\chi)\beta_m + \chi\beta_g$, where $\beta_g = 1/T_{gas}$ is the thermal expansion coefficient of ideal gas. K_u and K_m are the undrained and drained bulk moduli which also depend on the gas volume fraction χ (see Appendix A5 and Table A1). The equilibrium condition, Darcy's law, mass conservation, and energy conservation are (Kaviany, 2012)

$$\nabla \cdot \sigma_{ij} = 0 \tag{2a}$$

$$\vec{q} = -\frac{\kappa}{\eta_f}\nabla P \tag{2b}$$

$$\frac{\partial \zeta}{\partial t} + \nabla \cdot \vec{q} = 0 \tag{2c}$$

$$\frac{\partial T}{\partial t} + \frac{\rho_f c_f}{\rho_m c_m}\vec{q} \cdot \nabla T - c_{thermal}\nabla^2 T = 0 \tag{2d}$$

where $\vec{q}$ is Darcy's flow velocity, κ is the permeability of the mush, η_f is magma viscosity. (ρ_f, c_f) and (ρ_m, c_m) are the density and specific heat of the fluid phase and of the whole mush ensemble, respectively. $c_{thermal}$ is the thermal diffusivity in the mush. The boundary conditions include continuity of fluid pressure and radial stresses at r_o and R_o, and vanishing heat/fluid flow at R_o after the injection (see Appendix Appendix A). At $t > 0$, the evolution for displacement, pressure, stress, and fluid content are solved numerically using a finite difference scheme (see Appendix A2 for details). The solutions for the isothermal case are compared to the analytical solutions in Liao et al. (2021) for proper choice of time-step size.

Table A1 shows the values used in the study (Appendix A). In the examples shown below we assume that the two boundaries of the mush shell are at $T_{in} = 850^oC, T_{out} = 800^oC$ to be consistent with petrological evidence (Scarrow et al., 2021; Rout et al., 2021). This temperature range is also consistent with mush porosity of $20-30\%$ assumed in our study (Appendix Figure A2). Some petrological observations suggest lower mush storage temperatures (solidus or sub-solidus temperature near 700^oC), which do not change our findings qualitatively.

The timescales of the three dynamic processes are governed by different material properties of the crystal mush, including the viscoelastic relaxation time $\tau_r = \eta/\mu$, poroelastic diffusivity c_{poro} (see Table A1), and thermal diffusivity $c_{thermal}$. The three values, together with the characteristic size of the chamber r_o, lead to two ratios that reflect the relative rapidness: the ratio between thermal and poroelastic diffusivity $C \equiv c_{thermal}/c_{poro}$, and $r_o/[l]$ where the intrinsic material length scale $[l] \equiv \sqrt{\tau_r c_{poro}}$. Based on existing studies and assumptions made in our previous models (see Appendix §A5), $C \in [4 \times 10^{-6}, 3 \times 10^{-2}]$. In the examples shown below, we assume $r_o/[l] \sim 1$, which suggests that the poroelastic diffusion and viscoelastic relaxation occur with comparable rapidness across the mush.

2.2 Assumptions and caveats

The quantitative framework above is based on several assumptions which facilitate computation and comparison between our current model and previous studies. Below are discussions on these assumptions, as well as their implications on the application of the model.

a Symmetry and uniform material properties: following several previous studies, we assume radial symmetry for all quantities, and uniform material properties in the surrounding crust. These assumptions are made to rule out the contributions from regional tectonic setting and crustal heterogeneities. Several key material properties of crystal mush, such as porosity and permeability, are assumed to be uniform across the mush shell. Realistically, variation in temperature leads to variation in crystallinity, hence both porosity and permeability may vary radially. We estimate the range of porosity $\phi \sim \frac{T-T_{liq}}{T_{sol}-T_{liq}}$ and permeability $\kappa \propto \phi^2$, and find that, for solidus and liquidus temperature at 1100 and 600 degrees and a temperature range of $800^oC - 850^oC$, the variation in porosity and permeability are small and below one order of magnitude (Appendix A5 Figure A2). For convenience we therefore assume these values to be uniform across the mush shell.

b Limited dynamics of exsolved gas: Our model does not distinguish multicomponent gas vapor from single component vapor, and processes that may significantly alter the gas content are not considered. If the gas volume fractions are sufficiently large, pathways for gas flows may be formed and the magma chamber may become an open system to exsolved volatiles. In this scenario, additional physical processes for both the chamber and the crust are required to capture the transport of gas to the surface, as suggested by Mittal and Richards (2019). These processes are not within the scope of our current model, which is applicable only to low gas volume fractions which ensure the existence of exsolved gas in the form of isolated gas bubbles trapped within the pore spaces and the liquid core. In the current model we assume that the gas fractions in the chamber remain constant during the injection and pore pressure change. We find that pore pressure fluctuation on the scale of 1MPa does not significantly alter the exsolved gas volume fraction (see Appendix §A4 and Figure A1). For higher pore pressure perturbation (above 10Mpa) however, the re-absorption of exsolved gas could become non-negligible and need to be considered.

c Assumption of chamber insulation: our model does not consider the heat exchange between the magma chamber and the hosting country rock following the injection (i.e., the heat added by the injection is exchanged between the magma and mush much faster than between the mush and hosting rocks), hence the magma chamber is effectively insulated from the surrounding rocks at the onset of the injection, due to the lack of advective heat in the rocks and relative small temperature perturbation associated to the injection (on the scale of 10^oC) which has the sharpest gradient close to the core-mush interface.

d Instantaneous injection process: In our current model, we focus on fast injection events and magma mixing in the fluid core, which instantly cause pressure and temperature rise in the magma core. Other dynamics in a more realistic injection process, such as gradual injection and pressure-dependent injection volume flux may alter the response of the chamber by shortening the short-period evolution (Liao et al., 2021), or cause additional delays due to magma mixing in the core.

e Rheology: In this study we follow our earlier work and adopt a linear thermo-poro-viscoelastic rheology. This rheology combines classic Biot poroelastic theory, Maxwell relaxation model, and additional pore pressurization from thermal expansion/contraction. With this rheology, viscous relaxation of the mush occurs in the shear component (i.e., infinite bulk viscosity), hence omitting the compaction effect. The thermal expansion is restricted to the fluid components, as the thermal expansion coefficient for magma (especially gas bearing magma) is typically several times higher than that of solid crystals (Suzuki, 1975). For higher temperature and less compressible magma, however, a nonzero value for β_s could be required to describe the thermal effect more precisely. While there is a lack of direct measurements, processes not assumed in our current rheology, such as compaction, plastic deformation, shear localization and grain size evolution could potentially be important for the mush system, which require more modeling and measurements to verify in future studies.

3 Results

The injection is modeled by a sudden addition of hotter magma into the fluid core, which instantaneously elevates the chamber's pressure and temperature. Following the sudden injection, the pressure gradient, temperature gradient, and deviatoric stress in the mush leads to transport of magma, thermal diffusion, and viscoelastic relaxation. Figure 2 shows the examples for time-dependent evolutions of various quantities in the system following a sudden injection of magma, for both isothermal and non-isothermal cases. We examine several cases with regard to gas content: gas free, 10vol% gas in the core magma only, 10vol% gas in the pore magma only, and gas-rich (30vol% gas in pore magma and 10vol% gas in core magma). For a gas-rich chamber, the higher gas content in the mush is rationalized by its high crystallinity, which promotes gas exsolution (see §A4 and Figure A1a for the estimation of gas volume fractions.) These volume fractions are also broadly consistent with the observed 1-10wt% gas fraction reported in some studies (Figure A1b) (Wallace, 2001; Edmonds et al., 2014; Edmonds & Wallace, 2017).

When the magma chamber has uniform temperature, its behavior following an isothermal injection (i.e., injected magma has the same temperature as the fluid core) can be defined by a short-term evolution regime and a long-term evolution regime, as shown in (Liao et al., 2021). With the addition of a pre-injection temperature gradient across the mush and a hot injection (i.e., injected magma is hotter than the core magma), the model results reveal three regimes in the post-injection evolution (Figure 2). Below we describe the qualitative behavior of the mushy magma chamber during each of these periods.

3.1 Short-term evolution

The injection creates a gradient in fluid pressure across the core-mush boundary, with highest pressure in the fluid core. The short-term evolution is defined by the period of time during which magma is flowing ('leaks') from the core into the mush, driven by the pressure gradient. This period is primarily governed by mechanical processes; hence the isothermal and non-isothermal cases show very similar behaviors. With the non-isothermal cases, the transport of magma (Figure 2c) and the chamber's deformation (Figure 2a) are enhanced, because the thermal expansion of the heated core generates additional pressurization that drives magma transport.

During this period, the fluid pressure in the core is higher than the pore pressure in the mush, maintaining the outward transport of magma across the core-mush boundary (i.e., increasing M_{leak}, Figure 2c). As magma leaks into the mush, the core shrinks and the mush thickens. The displacement at the chamber's wall (hence the tensile stress and the ground elevation) results from the competing effects of the shrinking core and the expanding mush. The chamber's deformation hence is strongly tied to the distribution of gas, which determines the relative compressibility. When the fluid core is more compressible than the mush (e.g., gas-rich core and gas-poor mush), the magma transport results in larger volumetric expansion of the mush and smaller volumetric contraction of the core, leading to expansion of the whole chamber (i.e., increase in tensile stress); when the mush is more compressible than the core (e.g., gas-rich mush and gas-poor core), the core contraction dominates the mush expansion, leading to contraction of the whole chamber following the injection, hence decreasing tensile stress (Figure 2a). The transport of magma is promoted by higher gas content in the mush: a more compressible mush shell takes longer to be pressurized, hence maintaining the pressure gradient between the core and the mush for a longer time, pumping more magma from the core into the mush, and causing larger pressure loss in the core (Figure 2b, c). This observation holds true for both isothermal and non-isothermal injection. With a pre-injection thermal gradient and a hot injection event, the additional pressurization of the core resulting from thermal expansion promotes magma transport; this effect is most obvious when the system is gas rich, hence has higher thermal expansion coefficients.

3.2 Mid-term evolution

The mid-term evolution emerges as viscous relaxation becomes dominant. During the short-term evolution, the positive fluid pressure at the core-mush interface (i.e., higher core pressure) maintains magma transport from the core to the mush. The viscous relaxation causes the core-mush interface to creep outward and reduces the core pressure further. The onset of the mid-term evolution is defined by the moment when the core pressure drops below the pore pressure in the mush, causing the magma transport to reverse (i.e., onset of the decrease of M_{leak}, Figure 2c). The end of the mid-term evolution is defined by the e-folding time of the isothermal case, when the system approaches a new isothermal steady state (Liao et al., 2021). In this period of time, the viscous relaxation causes both the core-mush interface and the mush-rock interface to creep outward, leading to decrease in core pressure and increase in crustal stresses. When the system is isothermal, the gas content in the system does not qualitatively change the behavior of the chamber. The root cause for the system's distinct behavior at the beginning of the mid-term evolution is the coexistence of the porous flows with viscous relaxation: although the porous flows tend to eliminate pore pressure gradient, they do not eliminate the deviatoric stresses in the crystalline framework, hence the relaxation (outward displacement of the core-mush boundary) does not respond to equilibrating pore pressure; meanwhile, the relaxation of the mush frame, while eliminating deviatoric stress, does not eliminate pore pressure gradient. This discordance causes the non-monotonic transport of magma we observe.

The influence of gas and heat become more obvious in the middle of the mid-term evolution, when the core has lost sufficient heat to the mush (e.g., when the core temperature approaches its pre-injection value, Figure 2d). The core contracts due to cooling, with further decrease in core pressure (Figure 2b); the mush expands due to heating and pore pressure continues increasing. The thermal contraction of the core magma and the thermal expansion of the pore magma enhance the inverse transport of magma initiated by the viscous relaxation, leading to more magma being leaked back into the core, especially for gas-rich systems with higher thermal expansion coefficients (Figure 2c). In most cases, the thermal contraction of the core results in an inward retraction of the chamber's wall and a reduction of the crustal stresses, which is most prominent when the chamber has a gas-rich core and gas-poor mush. One exception is the case of a chamber with gas-rich mush and a gas-poor core, wherein the contraction of the core is offset by the thermal expansion of the mush, resulting in seemingly unchanged chamber deformation (Figure 2a).

3.3 Long-term evolution

The long-term evolution of the system is driven by thermal equilibration between the core and mush, which eventually ends when the temperature becomes uniform. This regime is an extension of the mid-term regime, where heat transport causes inverse pressure gradient to transport more magma from the mush to the core, further shrinking of the core and the chamber. In this regime, the pressure gradient that drives fluid flows is a consequence of thermal expansion and contraction, hence the system is driven thermally instead of mechanically. In our study we factored in the heat transport due to advection (i.e., carried by the porous flows), however, due to the constraint of the impermeable outer boundary, advective heat is very limited and thermal evolution is primarily driven by diffusion. In the examples shown in Figure 2, we assume the thermal diffusivity to be 4 orders of magnitude smaller than the poroelastic diffusivity, based on material properties assumed in previous studies (Appendix A5). We note that for larger thermal diffusivity, the thermal equilibration process occurs earlier and catches up with the mechanical equilibration process. In this case, the mid-term evolution and long-term evolution merges, and the system reaches thermal-mechanical steady state faster (Fig 3).

3.4 Competition between different rheological processes

The behavior of thermo-poroviscoelastic mush is a combined result of the two rheological end-members of thermo-poroelasticity and thermo-viscoelasticity. The thermo-poroelasticity end-member corresponds to a crystal mush with no viscoelastic relaxation; the viscoealstic end-member corresponds to crystal mush with no fluid flows (e.g., with vanishing permeability). While in previous sections we showed results for mush systems with comparable timescale for poroelastic and viscoelastic processes, realistic magma mushes may have faster poroelastic process or faster viscoelastic process (for example, for very falsic magma with high viscosity, or very high crystallinity with very low permeability, both could increase the poroelastic diffusion time by orders of magnitude). In the thermo-viscoelastic case, both interfaces continue to creep outward under relaxation initially, before they reverse direction due to cooling (Figure 4 a,b). In the thermo-poroelastic end-member, both interfaces continue to retract inward due to the transport of magma from the less compressible core to the more compressible mush (for the example of gas rich chamber); the magma initially leaks from the core to the mush but reverses direction later due to temperature equilibration (Figure 4c). The two rheological endmembers show opposite trends of tensile stress (Figure 4a); the non-monotonic time-dependent evolution for the thermo-poroviscoelastic case is therefore a product of the opposite trends set by the two different rheologies (Figure 2a).

4 Summary and Discussion

We examined the dynamics of a closed-system, mushy, and gas-bearing magma chamber subjected to a non-isothermal magma injection event. The study is based on existing isothermal models of mushy magma chambers (Liao et al., 2018, 2021). The magma chamber is modeled as a thermally insulated sphere consisting of a fluid core and a mush shell. The new aspects of gas and heat are reflected by the inclusion of a pre-injection thermal gradient in the mush shell, the injection of hotter magma, the thermal expansion/contraction of gas and magma and the temperature evolution following the injection. We find that following a sudden injection, the time evolution of chamber deformation, stress, and magma transport can be grouped broadly into three regimes, which are caused by (short-term) poroelastic diffusion, (mid-term) viscoelastic relaxation, and (long-

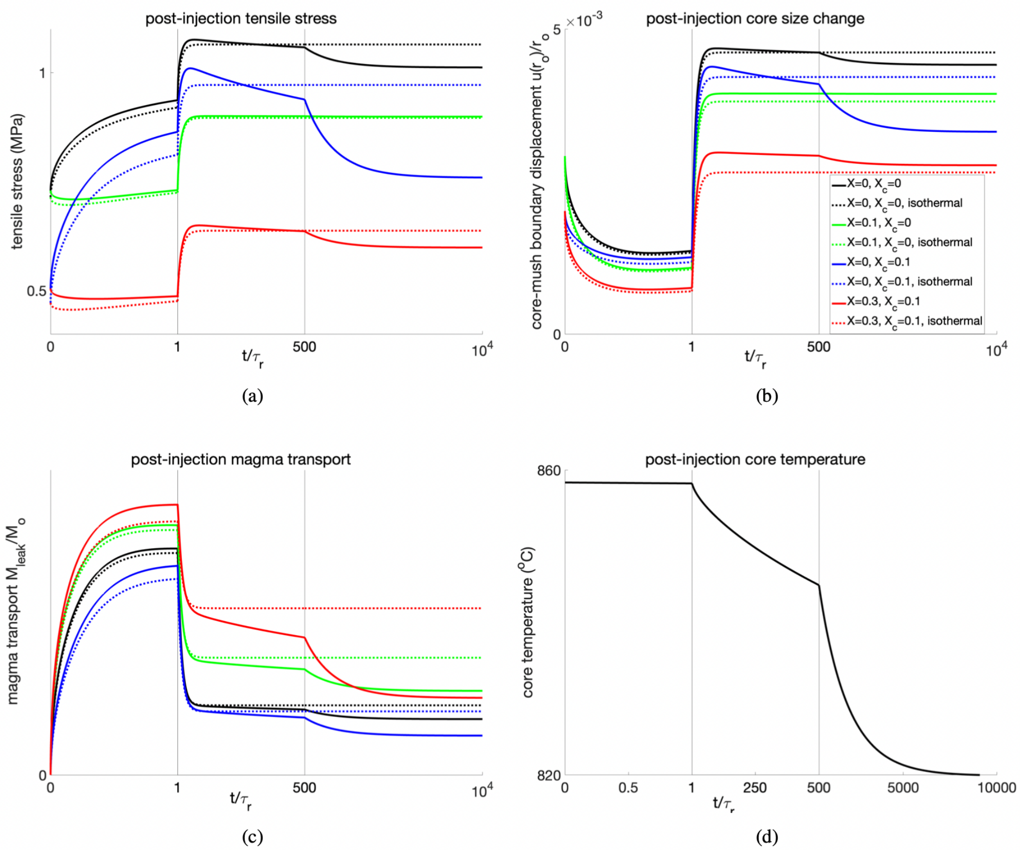

Figure 2. Example of evolution of the system following a sudden injection. The pre-injection temperature is 850^oC in the fluid core and 800^oC at the chamber's wall. At $t = 0$ a sudden injection occurs. A 2vol% of new injected magma, which is 50% hotter than the core magma, is added into the core and leads to an overall temperature increase of 8^oC. The system has geometry of $R_o = 2r_o$, characteristic length $[l] = \sqrt{c_{poro}\tau_r} = r_o$, and poroelastic diffusivity 4 orders of magnitude larger than thermal diffusivity with $C = 10^{-4}$. X-axis indicate piecewise linear post-injection time t, normalized by τ_r, and shown in three different ranges that illustrate the short-term, mid-term and long-term evolution time.

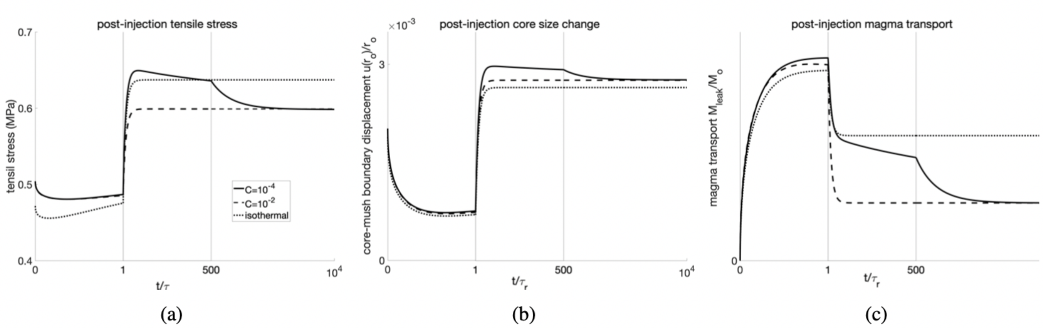

Figure 3. Post-injection evolution for two different thermal diffusivity and isothermal case. For slower thermal diffusion the ratio of thermal diffusivity to poroelastic diffusivity $c_{thermal}/c_{poro} = 10^{-4}$; for faster thermal diffusion $c_{thermal}/c_{poro} = 10^{-2}$. Other parameters are the same as in Figure 2, with gas content $X = 0.3, X_c = 0.1$.

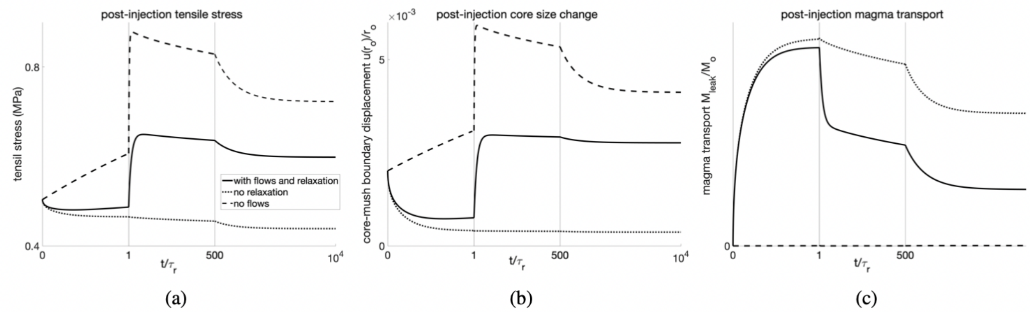

Figure 4. Post-injection evolution for different rheologies. Solid lines indicate thermo-poroviscoelastic mush where porous flows and matrix relaxation both exist; dashed lines indicate thermo-viscoealstic mush which corresponds to undrained/impermeable mush with no porous flows; dotted lines indicate thermo-poroelastic mush where relaxation is prohibited. The parameters used are the same as Figure 2 with $X = 0.3, X_c = 0.1$.

term) thermal equilibration. Gas in the pore space in the crystal mush promotes magma transport, lowers the deformation and stress, and may cause additional non-monotonic time-evolution of crustal stresses. By examining the end-member cases (no flows in the mush, or no relaxation), we find that the non-monotonic behavior of the chamber is a result of the competing processes of poroelasticity and viscoelasticity, as well as the contrasts in compressibility of the mush and core.

Our model does not simulate ground deformation explicitly. For magma chambers relatively deep (depth $> 2.5R_o$), the amplitudes of ground deformation are linear to the tensile stress (Liao et al., 2021; Segall, 2016). The time-dependent features of the tensile stress evolution are therefore identical to those of the ground deformation (i.e., increasing tensile stress corresponds to ground uplift, decreasing tensile stress corresponds to ground subsidence). The sensitive dependence of gas content in either isothermal or non-isothermal cases implies the intrinsic ability for a mushy magma chamber to generate complex time-sequences of ground deformation without requesting non-monotonic injections. Specifically, a system with gas rich mush and a gas poor core develops the obvious non-monotonic evolution of chamber wall displacement/tensile stress, which would lead to multiple episodes of ground elevation/subsidence following a sudden injection. Compared to isothermal case, the thermal evolution of the system leads to additional mid-to-long term chamber contraction, and promotes magma mixing by allowing more magma to flow between the core and the mush. As the gas content and gas distribution in the chamber could change with the chemical, thermal, and mechanical evolution of the reservoir, the same kind of magma injection event for the same magma chamber may result in very different time-series of ground elevation.

Crustal magmatic systems are complex, with irregular geometries, spatial heterogeneities, and coupled nonlinear processes that are challenging to model. In our present model, some aspects of the system are simplified, such as simplified model geometry (radial symmetry), uniform and/or constant material properties such as permeability, simplified dynamics of exsolved gas (i.e., only assume bubble suspension), and some simplifications on the thermal evolution (e.g., thermal insulation within the system). The injection process and the rheology are chosen to best align with previous studies for a clear illustration of the intrinsic dynamics of the system. Because of these simplifications, our model results are best suited for gaining understanding of the additional complexities of a mushy-and-gassy magma chamber.

5 Open Research

Codes for realizing the analytical and semi-analytical solutions have been submitted to open repository Code Ocean.

Acknowledgments
I thank Paul Segall and an anonymous reviewer for reviewing this manuscript and providing constructive feedbacks.

References

Annen, C., & Burgisser, A. (2021). Modeling water exsolution from a growing and solidifying felsic magma body. *Lithos*, *402*, 105799.

Bachmann, O., & Bergantz, G. W. (2006). Gas percolation in upper-crustal silicic crystal mushes as a mechanism for upward heat advection and rejuvenation of near-solidus magma bodies. *Journal of Volcanology and Geothermal Research*, *149*(1), 85 - 102. Retrieved from `http://www.sciencedirect.com/science/article/pii/S0377027305002076` doi: https://doi.org/10.1016/j.jvolgeores.2005.06.002

Biggs, J., & Annen, C. (2019). The lateral growth and coalesence of magma systems. *Philosophical Transactions of the Royal Society A: Mathematical, Physical and Engineering Sciences*, *377*(2139), 20180005. Retrieved from `https://royalsocietypublishing.org/doi/abs/10.1098/rsta.2018.0005` doi: 10.1098/rsta.2018.0005

Biot, M. A. (1941). General theory of three-dimensional consolidation. *Journal of applied physics*, *12*.

Browning, J., Drymoni, K., & Gudmundsson, A. (2015). Forecasting magma-chamber rupture at santorini volcano, greece. *Scientific Reports*, *5*, 15785. Retrieved from `http://www.ncbi.nlm.nih.gov/pmc/articles/PMC4623603/` doi: 10.1038/srep15785

Cashman, K. V., Sparks, R. S. J., & Blundy, J. D. (2017). Vertically extensive and unstable magmatic systems: A unified view of igneous processes. *Science*, *355*(6331). Retrieved from `http://science.sciencemag.org/content/355/6331/eaag3055` doi: 10.1126/science.aag3055

Cheng, A. H.-D. (2016). *Poroelasticity*. Springer International Publishing. doi: doi.org/10.1007/978-3-319-25202-5

Davis, M., Koenders, M., & Petford, N. (2007). Vibro-agitation of chambered magma. *Journal of Volcanology and Geothermal Research*, *167*(1), 24-36. Retrieved from `https://www.sciencedirect.com/science/article/pii/S0377027307002223` (Large Silicic Magma Systems) doi: https://doi.org/10.1016/j.jvolgeores.2007.07.012

Edmonds, M., Humphreys, M. C. S., Hauri, E. H., Herd, R. A., Wadge, G., Rawson, H., . . . Guida, R. (2014). Pre-eruptive vapour and its role in controlling eruption style and longevity at soufrière hills volcano. *Geological Society, London, Memoirs*, *39*(1), 291-315. Retrieved from `https://mem.lyellcollection.org/content/39/1/291` doi: 10.1144/M39.16

Edmonds, M., & Wallace, P. J. (2017, 02). Volatiles and exsolved vapor in volcanic systems. *Elements*, *13*(1), 29-34. Retrieved from `https://doi.org/10.2113/gselements.13.1.29` doi: 10.2113/gselements.13.1.29

Edmonds, M., & Woods, A. W. (2018). Exsolved volatiles in magma reservoirs. *Journal of Volcanology and Geothermal Research*, *368*, 13-30. Retrieved from `https://www.sciencedirect.com/science/article/pii/S0377027318302944` doi: https://doi.org/10.1016/j.jvolgeores.2018.10.018

Girona, T., Costa, F., & Schubert, G. (2015). Degassing during quiescence as a trigger of magma ascent and volcanic eruptions. *Scientific Reports*, *5*, 18212.

Retrieved from http://www.ncbi.nlm.nih.gov/pmc/articles/PMC4678897/ doi: 10.1038/srep18212

Gudmundsson, A. (2015). Collapse-driven large eruptions. *Journal of Volcanology and Geothermal Research*, *304*, 1 - 10. Retrieved from http://www.sciencedirect.com/science/article/pii/S0377027315002413 doi: https://doi.org/10.1016/j.jvolgeores.2015.07.033

Head, M., Hickey, J., Gottsmann, J., & Fournier, N. (2021). Exploring the impact of thermally controlled crustal viscosity on volcanic ground deformation. *Journal of Geophysical Research: Solid Earth*, *126*(8), e2020JB020724. Retrieved from https://agupubs.onlinelibrary.wiley.com/doi/abs/10.1029/2020JB020724 (e2020JB020724 2020JB020724) doi: https://doi.org/10.1029/2020JB020724

Huber, C., Bachmann, O., & Dufek, J. (2011). Thermo-mechanical reactivation of locked crystal mushes: Melting-induced internal fracturing and assimilation processes in magmas. *Earth and Planetary Science Letters*, *304*(3–4), 443 - 454. Retrieved from http://www.sciencedirect.com/science/article/pii/S0012821X11000938 doi: https://doi.org/10.1016/j.epsl.2011.02.022

Huppert, H. E., & Woods, A. W. (2002, 12 05). The role of volatiles in magma chamber dynamics. *Nature*, *420*(6915), 493–495. Retrieved from http://dx.doi.org/10.1038/nature01211

Jackson, M. D., Blundy, J., & Sparks, R. S. J. (2018). Chemical differentiation, cold storage and remobilization of magma in the earth's crust. *Nature*, *564*, 405-409.

Kaviany, M. (2012). *Principles of heat transfer in porous media.* Springer Science and Business Media.

Lerner, A. H., Wallace, P. J., Shea, T., Mourey, A. J., Kelly, P. J., Nadeau, P. A., ... Werner, C. A. (2021). The petrologic and degassing behavior of sulfur and other magmatic volatiles from the 2018 eruption of kilauea, hawaii: melt concentrations, magma storage depths, and magma recycling. *Bulletin of Volcanology*, *83*(6), 43. Retrieved from https://doi.org/10.1007/s00445-021-01459-y doi: 10.1007/s00445-021-01459-y

Liao, Y., Soule, S. A., & Jones, M. (2018, 2019/03/11). On the mechanical effects of poroelastic crystal mush in classical magma chamber models. *Journal of Geophysical Research: Solid Earth*, *123*(11), 9376–9406. Retrieved from https://doi.org/10.1029/2018JB015985 doi: 10.1029/2018JB015985

Liao, Y., Soule, S. A., Jones, M., & Le Mével, H. (2021). The mechanical response of a magma chamber with poroviscoelastic crystal mush. *Journal of Geophysical Research: Solid Earth*, *126*(4), e2020JB019395. Retrieved from https://agupubs.onlinelibrary.wiley.com/doi/abs/10.1029/2020JB019395 (e2020JB019395 2020JB019395) doi: https://doi.org/10.1029/2020JB019395

Métrich, N., & Wallace, P. J. (2008). Volatile abundances in basaltic magmas and their degassing paths tracked by melt inclusions. *Reviews in mineralogy and geochemistry*, *69*(1), 363-402.

Mittal, T., & Richards, M. A. (2019). Volatile degassing from magma chambers as a control on volcanic eruptions. *Journal of Geophysical Research: Solid Earth*, *124*(8), 7869-7901. Retrieved from https://agupubs.onlinelibrary.wiley.com/doi/abs/10.1029/2018JB016983 doi: 10.1029/2018JB016983

Mordensky, S. P., & Wallace, P. J. (2018). Magma storage below cascades shield volcanoes as inferred from melt inclusion data: A comparison of long-lived and short-lived magma plumbing systems. *Journal of Volcanology and Geothermal Research*, *368*, 1-12. Retrieved from https://www.sciencedirect.com/science/article/pii/S0377027317301026 doi: https://doi.org/10.1016/j.jvolgeores.2018.10.011

Nishimura, T. (2004). Pressure recovery in magma due to bubble growth. *Geophysical Research Letters*, *31*(12), n/a–n/a. Retrieved from http://dx.doi.org/10

.1029/2004GL019810 (L12613) doi: 10.1029/2004GL019810

Rout, S. S., Blum-Oeste, M., & Wörner, G. (2021). Long-term temperature cycling in a shallow magma reservoir: insights from sanidine megacrysts at taápaca volcano, central andes. *Journal of Petrology*, *62*(9).

Scarrow, J., Schmitt, A., Barclay, J., Horstwood, M., Bloore, A., & Christopher, T. (2021). Zircon as a tracer of plumbing processes in an active magmatic system: Insights from mingled magmas of the 2010 dome collapse, montserrat, lesser antilles arc, caribbean. *Journal of Volcanology and Geothermal Research*, 107390. Retrieved from https://www.sciencedirect.com/science/article/pii/S0377027321002195 doi: https://doi.org/10.1016/j.jvolgeores.2021.107390

Segall, P. (2016). Repressurization following eruption from a magma chamber with a viscoelastic aureole. *Journal of Geophysical Research: Solid Earth*, *121*(12), 8501–8522. Retrieved from http://dx.doi.org/10.1002/2016JB013597 (2016JB013597) doi: 10.1002/2016JB013597

Sparks, R. S. J., Annen, C., Blundy, J. D., Cashman, K. V., Rust, A. C., & Jackson, M. D. (2019). Formation and dynamics of magma reservoirs. *Philosophical Transactions of the Royal Society A: Mathematical, Physical and Engineering Sciences*, *377*(2139), 20180019. Retrieved from https://royalsocietypublishing.org/doi/abs/10.1098/rsta.2018.0019 doi: 10.1098/rsta.2018.0019

Srigutomo, W., Trimadona, Martakusumah, R., & Anwar, H. (2015). Modeling and inversion of volcanic surface deformation based on mogi model and mctigue model. *AIP Conference Proceedings*, *1656*(1), 070016. Retrieved from http://aip.scitation.org/doi/abs/10.1063/1.4917162 doi: 10.1063/1.4917162

Suzuki, I. (1975). Thermal expansion of periclase and olivine, and their anharmonic properties. *Journal of Physics of the Earth*, *23*(2), 145-159.

Tallarico, A., Dragoni, M., Anzidei, M., & Esposito, A. (2003). Modeling long-term ground deformation due to the cooling of a magma chamber: Case of basiluzzo island, aeolian islands, italy. *Journal of Geophysical Research: Solid Earth*, *108*(B12). Retrieved from https://agupubs.onlinelibrary.wiley.com/doi/abs/10.1029/2002JB002376 doi: 10.1029/2002JB002376

Townsend, M. (2022). Linking surface deformation to thermal and mechanical magma chamber processes. *Earth and Planetary Science Letters*, *577*, 117272. Retrieved from https://www.sciencedirect.com/science/article/pii/S0012821X21005288 doi: https://doi.org/10.1016/j.epsl.2021.117272

Voight, B., Widiwijayanti, C., Mattioli, G., Elsworth, D., Hidayat, D., & Strutt, M. (2010). Magma-sponge hypothesis and stratovolcanoes: Case for a compressible reservoir and quasi-steady deep influx at soufrière hills volcano, montserrat. *Geophysical Research Letters*, *37*(19).

Wallace, P. (2001). Volcanic so 2 emissions and the abundance and distribution of exsolved gas in magma bodies. *Journal of Volcanology and Geothermal Research*, *108*(1).

Wasser, V. K., Lopez, T. M., Anderson, K. R., Izbekov, P. E., & Freymueller, J. T. (2021). Multidisciplinary constraints on magma compressibility, the pre-eruptive exsolved volatile fraction, and the h2o/co2 molar ratio for the 2006 augustine eruption, alaska. *Geochemistry, Geophysics, Geosystems*, *22*(9), e2021GC009911. Retrieved from https://agupubs.onlinelibrary.wiley.com/doi/abs/10.1029/2021GC009911 (e2021GC009911 2021GC009911) doi: https://doi.org/10.1029/2021GC009911

Whitney, J. A. (1988). The origin of granite: The role and source of water in the evolution of granitic magmas. *Geological Society of America Bulletin*, *100*(12), 1886-1897.

Table A1. Symbols of the constants used in the study

	symbol	definition	typical value/expression
constants	P_{abs}	absolute pressure of the system	100MPa (5km)
	T_{in}	pre-injection absolute temperature in the fluid core	850^oC
	T_{out}	pre-injection absolute temperature at chamber boundary	800^oC
	r_o	radius of liquid magma core at initial steady state	0.1–5 km
	R_o	radius of magma chamber at initial steady state	$2r_o$
	α	poro-elastic coefficient (Biot coefficient) of the mush	0.6, 0.9
	ϕ_o	porosity in mush at initial steady state	0.3
	χ	pore gas volume fraction	0-0.3
	K_s	elastic bulk modulus of solid crystals	10GPa
	K_l	bulk modulus of pure magma	1Gpa
	β_l	volumetric thermal expansion coefficient of pure magma	$5 \times 10^{-5}/^oC$
	K_g	bulk modulus of gas	P_{abs}
	β_g	volumetric thermal expansion coefficient of gas	$1/T_{in}$
	β_s	volumetric thermal expansion coefficient of crystals	0
	K_{core}	bulk modulus of the core	$1/(\chi_c/K_g + (1-\chi_c)/K_l)$
	β_{core}	volumetric thermal expansion coefficient of the core	$\chi_c\beta_g + (1-\chi_c)\beta_l$
	K_{pore}	bulk modulus of pore magma	$1/(\chi/K_g + (1-\chi)/K_l)$
	β_{pore}	volumetric thermal expansion coefficient of the pore	$\chi\beta_g + (1-\chi)\beta_l$
	K_m	drained bulk modulus of mush	$(1-\alpha)K_s$
	K_u	undrained bulk modulus of mush	$(1-\alpha)K_s + \frac{\alpha^2 K_s K_{pore}}{\phi_o K_s + (\alpha-\phi_o)K_{pore}}$
	η_f	viscosity of pore magma	10^2–10^6Pa.s
	κ	permeability in mush	10^{-10}–$10^{-8}m^2$
	μ	instantaneous shear modulus of host rock and mush	1GPa
	η	viscosity of the mush ensemble	$10^{16} - 10^{18}$Pa.s
	τ_r	relaxation time	η_m/μ
	M_o	total mass in the liquid core before injection	value not used
	ΔM	total mass injected into the chamber	$02\%M_o$
	$[l]$	characteristic time	$\sqrt{\tau_r c}$
	ρ_f	magma density	value not used
	ρ_m	crystalline matrix density	value not used
	c_f	magma specific heat	value not used
	c_m	crystalline matrix specific heat	value not used
	δ	dimensionless value $\delta \equiv c_f\rho_f/c_m\rho_m$	1
	c_{poro}	poro-elastic diffusivity	$\frac{\kappa}{\eta_f}\frac{(K_m+\frac{4}{3}\mu)(K_u-K_m)}{\alpha^2(K_u+\frac{4}{3}\mu)}$
	$c_{thermal}$	thermal diffusivity in much	value not used
	C	dimensionless value $C \equiv c_{thermal}/c_{poro}$	$10^{-2}, 10^{-4}$
variables	σ_{ij}	stress tensor	
	ϵ_{ij}	strain tensor	
	ϵ	volumetric strain	$Tr(\epsilon_{ij})$
	P	pore pressure	
	ζ	variation of fluid content	Eq 1b
	$\vec{q}$	Darcy's flow velocity	Eq 2b
	T	temperature increment from reference value	

Appendix A Governing equations and solution method

A1 Normalization and solution scheme

We define a characteristic time scale $[t]$, characteristic length scale $[l]$, and temperature scale $[T]$ to normalize the variables in the system. The characteristic time and length scale are related via the instantaneous poroelastic diffusivity $[t] = \frac{[l]^2}{c}$ (when porous flows are allowed). We further choose $[t] = \tau_r = \eta/\mu$, which lead to the intrinsic length scale $[l] = \sqrt{\tau_r c}$. We can show that for a system with a characteristic size larger than $[l]$, the viscous relaxation is faster than the poroelastic diffusion; for a system with size smaller than $[l]$, the poroelastic diffusion is faster than viscous relaxation. The example we choose to examine with the model has a characteristic size $r_o = [l]$, indicating that for the mush shell, the viscoelastic relaxation and poroelastic diffusion occur at similar rate. When the system is thermo-poroelastic (i.e., no relaxation), $\tau_r = \infty$ and the timescale is determined by the system's dimension $[t] = r_o^2/c$; when the system is thermo-viscoelastic (i.e., no fluid flows), the length scale is defined by thermal diffusivity instead $[l] = \sqrt{\tau_r \kappa_T}$.

Using the characteristic scales we can write the constitutive relations (1) and the equilibrium condition (2) in their dimensionless forms in spherical coordinates with radial symmetry (all quantities are normalized except for pressure/stress, $\dot{}$ indicates time derivative)

$$\frac{[t]}{\tau_r}(K\epsilon - \alpha P) + (K + \frac{4}{3}\mu)\dot{\epsilon} - \alpha \dot{P} = F(t) \tag{A1a}$$

$$\dot{\sigma}_{rr} + \frac{[t]}{\tau_r}\sigma_{rr} = F - 4\mu\frac{\dot{u}}{r} \tag{A1b}$$

$$\dot{T} + \delta q_r \frac{\partial T}{\partial r} - \frac{\kappa_T}{c}\nabla^2 T = 0 \tag{A1c}$$

$$q_r = -\frac{\alpha^2 B(1-B)}{A-B}\frac{\partial P/\partial r}{K} \tag{A1d}$$

$$\dot{\zeta} = -\frac{1}{r^2}\frac{\partial}{\partial r}(r^2 q_r) \tag{A1e}$$

$$\dot{P} + b_1 P = b_2\dot{\zeta} + b_3\zeta + b_4\dot{T} + b_5 T + b_6 F(t) \tag{A1f}$$

$$\dot{\epsilon} + a_1\epsilon = a_2\dot{\zeta} + a_3\zeta + a_4\dot{T} + a_5 T + a_6 F(t) \tag{A1g}$$

where $F(t)$ is a time-dependent function,

$$A \equiv \frac{K_u}{K_u + \frac{4}{3}\mu}, \quad B \equiv \frac{K_m}{K_m + \frac{4}{3}\mu}, \quad \delta \equiv \frac{(\rho c)_{fluid}}{(\rho c)_{mixure}}, \quad \beta \equiv \phi_o \beta_f [T]$$

$$a_1 = \frac{[t]}{\tau_r}A, \quad a_2 = \frac{1}{\alpha}\frac{A-B}{1-B}, \quad a_3 = \frac{[t]}{\tau_r}a_2, \quad a_4 = \beta a_2, \quad a_5 = \frac{[t]}{\tau_r}\beta a_2, \quad a_6 = (A - \frac{A-B}{1-B})\frac{1}{K_m}$$

$$b_1 = \frac{[t]}{\tau_r}A, \quad b_2 = \frac{1}{\alpha^2}\frac{A-B}{B(1-B)}K_m, \quad b_3 = \frac{[t]}{\tau_r}\frac{K_m}{\alpha^2}\frac{A-B}{1-B}, \quad b_4 = \beta b_2, \quad b_5 = \beta b_3, \quad b_6 = -\frac{1}{\alpha}\frac{A-B}{1-B}$$

A2 Solution scheme

The governing equations in Eq A1 are closed by boundary conditions at the core-mush and mush-rock interface, as well as the equation of state for the core magma.

At the core-mush interface, the boundary conditions include continuity of temperature, fluid pressure, displacement, and stress (i.e., force balance). Substituting fluid pressure continutiy to the constitutive relation at the inner boundary of the mush shell leads to

$$\dot{P}_c + b_1 P_c = b_2\dot{\zeta}(r_o) + b_3\zeta(r_o) + b_4\dot{T}_c + b_5 T(r_o) + b_6 F(t) \tag{A2}$$

Substituting the stress continuity (force balance) to the stress-strain relation at the inner boundary leads to

$$\frac{\dot{u}(r_o)}{r_o} = \frac{\dot{P}_c}{4\mu} + \frac{[t]}{\tau_r}\frac{P_c}{4\mu} + \frac{F}{4\mu} \tag{A3}$$

At the mush-rock interface, displacement and radial stress are continuous and fluid flow vanishes (i.e., crust is impermeable to magma). We assume that the chamber is bounded by infinite domain of crustal rock with rigidity μ_{crust}, hence the radial stress in the hosting rock $\sigma_{rr} = -4\mu_{crust}\frac{u}{r}$. Substituting the stress and displacement continuity to the stress-strain relation at the outer boundary of the mush shell and assuming $\mu_{crust} = \mu$ we obtain

$$F(t) = -4\mu\frac{[t]}{\tau_r}\frac{u(R_o)}{R_o} \tag{A4}$$

The impermeable boundary (no flow) condition at the mush-rock interface is used for obtaining the displacement at the boundary: integrating for displacement using the relation $\dot{\epsilon} = \frac{1}{r^2}\frac{\partial(r^2\dot{u})}{\partial r} = -a_1\epsilon + a_2\dot{\zeta} + a_3\zeta + a_4\dot{T} + a_5 T + a_6 F(t)$, the mass conservation $\dot{\zeta} = -\frac{1}{r^2}\frac{\partial}{\partial r}(r^2 q_r)$, and the no-flow boundary condition $q_r(R_o) = 0$, we obtain the increment for displacement at the outer boundary

$$\frac{\dot{u}(R_o)}{R_o} = \frac{r_o^3}{R_o^3}\frac{\dot{u}(r_o)}{r_o} + \frac{1}{R_o^3}\int_{r_o}^{R_o}(a_3\zeta + a_4\dot{T} + a_5 T)r^2 dr - a_1\left(\frac{u(R_o)}{R_o} - \frac{r_o^3}{R_o^3}\frac{u(r_o)}{r_o}\right) + \frac{a_6 F(t)}{3}\left(1 - \frac{r_o^3}{R_o^3}\right) + a_2\frac{r_o^2}{R_o^3}q(r_o)$$

The magma within the fluid core obeys mass conservation, which is approximated as (after linearization and normalization using pre-injection mass M_o, velocity scale $[l]/[t]$, and mass flux scale $M_o/[t]$)

$$\dot{M}_c = Q_{in} - \frac{3}{r_o}q(r_o)$$

Substituting the mass conservation to the energy conservation equation in core magma leads to temperature change in core magma

$$\dot{T}_c = \frac{1}{M_c}\left(Q_{in}(T_{in} - T_c) + 3\frac{1}{\delta}\frac{\kappa_T}{c}\frac{1}{r_o}T'(r_o)\right)$$

where the first term on the Right-Hand-Side is the contribution of the (hotter) injected magma; the second term on the RHS is the contribution from heat removal by the cooler mush.

To obtain the pressure evolution of the core magma we use the equation of state in combination with the core-mush boundary condition. Combining $\dot{M} = \frac{d(\rho V)}{dt} = \rho\dot{V} + \rho V(\frac{\partial\rho}{\rho\partial T}\dot{T} + \frac{\partial\rho}{\rho\partial P}\dot{P})$, the stress-strain relation, and force balance $\sigma_{rr}(r_o) = -P_c$, we obtain (dimensionless; pressure is normalized by μ)

$$\dot{P}_c = \frac{1}{\frac{\mu}{K_l} + \frac{3}{4}}\left(\beta_l[T]\dot{T}_c + \dot{M}_c - \frac{3}{4}F - \frac{3}{4}\frac{[t]}{\tau_r}P_c\right)$$

The evolution for pressure, temperature and mass in the core magma are used to close the evolution equations. The energy equation and pore diffusion equations are solved in matlab with a finite difference scheme, on a 1D grid with $\Delta r = (R_o - r_o)/100$ with time step $\Delta t = \Delta r^2/2$. Below are the steps for iterating the solutions with boundary conditions at each time step: (all values are dimensionless, $'$ denotes gradient)

0 Setting initial values (see next section)
1 Solve for fluid velocity. $q = -\frac{\alpha^2 B(1-B)}{B-A}\frac{\mu}{K}P'$
2 Solve for core mass increment $\dot{M}_c = Q_{in} - \frac{3}{r(1)}q(1)$ ($q^{(1)}$ is displacement on the inner interface $r_o = 1$).
3 Solve for (dimensionless) chamber temperature increment $\dot{T}_c = \frac{1}{M_c}\left(Q_{in}(T_{in} - T_c) + 3\frac{1}{\delta}\frac{c_{thermal}}{c_{poro}}\frac{1}{r_o}T'(r_o)\right)$
4 get $F(t) = -4\frac{[t]}{\tau_r}\frac{u(R_o)}{R_o}$

5 get $\dot{P}_c = \frac{1}{\frac{\mu}{K_{core}}+\frac{3}{4}}\left(\beta_{core}[T]\dot{T}_c + \dot{M}_c - \frac{3}{4}F - \frac{3}{4}\frac{[t]}{\tau_r}P_c\right)$

6 get $\frac{\dot{u}(r_o)}{r_o} = \frac{\dot{P}_{ch}}{4} + \frac{\tau_d}{\tau_r}\frac{P_{ch}}{4} + F(t)/4$

7 get $\dot{T}$ in the shell (advection diffusion equation) with boundary value $\dot{T}_c$ and assuming temperature gradient at the outer boundary is 0 (chamber is insulated from the crust) $\dot{T} + \delta q_r T' - \frac{c_{thermal}}{c_{poro}}\nabla^2 T = 0$

8 get $\frac{\dot{u}(R_o)}{R_o} = \frac{r_o^3}{R_o^3}\frac{\dot{u}(r_o)}{r_o} + \frac{1}{R_o^3}\int_{r_o}^{R_o}(a_3\zeta + a_4\dot{T} + a_5 T)r^2 dr - a_1(\frac{u(R_o)}{R_o} - \frac{r_o^3}{R_o^3}\frac{u(r_o)}{r_o}) + \frac{a_6 F(t)}{3}(1 - \frac{r_o^3}{R_o^3}) + a_2\frac{r_o^2}{R_o^3}q(r_o)$

9 get $\dot{\zeta}(r_o) = \frac{1}{b_2}\dot{P}_{ch} + \frac{b_1}{b_2}P_{ch} - \frac{b_3}{b_2}\zeta(r_o) - \frac{b_4}{b_2}\dot{T}(r_o) - \frac{b_5}{b_2}T(r_o) - \frac{b_6}{b_2}F(t)$

10 get $\dot{\zeta} = -\frac{1}{r^2}\frac{\partial(r^2 q)}{\partial r}$ with inner boundary value $\dot{\zeta}(r_o)$ given.

11 get (in shell) $\dot{\epsilon} = a_2\dot{\zeta} + a_3\zeta + a_4\dot{T} + a_5 T + a_6 F(t) - a_1\epsilon$

11 get (in shell) $\dot{P} = b_2\dot{\zeta} + b_3\zeta + b_4\dot{T} + b_5 T + b_6 F(t) - b_1 P$

12 Update values for next iteration for: M, T_{ch}, P_{ch}, $u(r_o)$, $u(R_o)$, ζ, T, ϵ, P.

A3 Initial conditions

The system prescribed by the equations of motion does not have a trivial initial condition due to the thermal-mechanical coupling, and hence needs to be solved analytically. In this section we show the solution for the various quantities in the system based on the non-uniform temperature distribution. We assume that there are two conditions met prior to an injection: first, the temperature in the core is constant at T_{in}, and the temperature in the mush obeys $\nabla^2 T = 0$; second, there is no fluid flow, hence pore pressure is uniform across the mush.

The temperature is obtained by solving for

$$\nabla^2 T(r) = 0, \quad T(r_o) = T_{in}, \quad T(R_o) = T_{out}$$

which leads to solution $T(r) = T_{in} - \frac{T_{in}-T_{out}}{\frac{1}{r_o}-\frac{1}{R_o}}(\frac{1}{r_o} - \frac{1}{r})$. After non-dimensionalization, the solution leads to 0-th order dimensionless temperature increment

$$T^{(0)}(r) = \frac{a}{r} + b, \quad a = \frac{T_{in} - T_{out}}{[T]}\frac{1}{\frac{1}{r_o} - \frac{1}{R_o}}, \quad b = \frac{T_{in} - T_{ref}}{[T]} - \frac{T_{in} - T_{out}}{[T]}\frac{1}{1 - \frac{r_o}{R_o}}$$

where $[T]$ is the temperature scale chosen for the system $[T] = 850^oC$, $T_{ref} = 850^oC$ is a reference temperature chosen for 0 thermal expansion.

The requirement of vanishing fluid flow indicates that at the initial steady state, the system is drained with uniform pore pressure $P(r) = P_o$ across the mush shell. The initial state can be viewed as a steady state solution (i.e. no time derivatives in the constitutive relations) with the prescribed temperature distribution. Assuming $\mu_c = \mu$, the relations in (A1b), (A3) and (A4) lead to uniform radial stress, chamber pressure, and chamber displacement

$$\sigma_{rr}(r) = -P_o, \quad P_c = P_o, \quad F = -\frac{[t]}{\tau_r}P_o, \quad \frac{u(R_o)}{R_o} = \frac{P_o}{4\mu}$$

The constitutive relation for pore fluid content (A1f) leads to

$$\zeta = \left(\frac{b_1}{b_3} + \frac{[t]}{\tau_r}\frac{b_6}{b_3}\right)P_o - \beta T = \left(\frac{\alpha^2}{K}\frac{A(1-B)}{A-B} - \frac{\alpha}{K}\right)P_o - \beta T$$

The magma transport between core and mush can be obtained by integrating the above expression

$$\frac{M_{leak}}{M_o} = \frac{3}{r_o^3}\int \zeta r^2 dr = \left(\frac{\alpha^2}{K}\frac{A(1-B)}{A-B} - \frac{\alpha}{K}\right)P_o(\frac{R_o^3}{r_o^3} - 1) - \frac{3\beta}{r_o^3}\left(\frac{a}{2}(R_o^2 - r_o^2) + \frac{b}{3}(R_o^3 - r_o^3)\right)$$

Substituting the expression for fluid content and temperature in (A1f) leads to uniform volumetric strain $\epsilon = \frac{\alpha-1}{K}P_o$, which is integrated to yield displacement

$$\frac{u(r_o)}{r_o} = \left(\frac{R_o^3}{r_o^3}\frac{1}{4\mu} + \frac{1-\alpha}{3K}(\frac{R_o^3}{r_o^3} - 1)\right) P_o$$

To close the problem and seek the actual value for P_o, the equation of state for core fluid is used $-\frac{M_{leak}}{M_o} = \frac{P_o}{K_l} + 3\frac{u(r_o)}{r_o}$, which leading to

$$P_o = \frac{cc}{dd}, \quad \frac{M_{leak}}{M_o} = bb(\frac{R_o^3}{r_o^3} - 1)P_o - cc, \quad \zeta = bbP_o - \beta T, \quad \frac{u(r_o)}{r_o} = aaP_o$$

where

$$aa = \frac{R_o^3}{r_o^3}\frac{1}{4\mu} + \frac{1-\alpha}{3K}(\frac{R_o^3}{r_o^3} - 1), \quad bb = \frac{\alpha^2}{K}\frac{A(1-B)}{A-B} - \frac{\alpha}{K}$$

$$cc = \frac{3\beta}{r_o^3}\left(\frac{a}{2}(R_o^2 - r_o^2) + \frac{b}{3}(R_o^3 - r_o^3)\right), \quad dd = \frac{1}{K_{core}} + 3aa + (\frac{R_o^3}{r_o^3} - 1)bb$$

We can observe that this set of initial conditions correspond to a mush that is uniformly strained, has non-vanishing pressure and stress, and has a non uniform distribution of fluid content and temperature. These non-trivial features (as opposed to trivial initial condition in previously models consisting of all uniform values prior to injection) are consequence of the non-uniform temperature and the thermal stresses imposed by the steady stated temperature profile. We find that the initial values have very small values, and remove them from the final post-injection state to show the time-dependent variations.

A4 Evaluation of gas content

The volume fraction of exsolved gas in the core and pore magmas are free variables in the model and may have strong variations depending on depth, temperature, injection/eruption history, and ways the mush is formed. Here we provide justification for one case of gas fractions assumed in the main text ($\chi = 0.3, \chi_c = 0.1$) by evaluating exsolved gas fraction following in-situ crystalization and exsolution. Assuming that prior to gas exsolution and crystalization, the dissolved volatile concentration is c_o (mass fraction). After gas exsolution and crystalization, the dissolved volatile concentration is c in magma, and $c_{crystal} \approx 0.4wt\%$ in the crystals (Whitney, 1988; Annen & Burgisser, 2021). The volume of (pure) magma, exsolved gas, and crystals are V_m, V_g, V_c; all exsolved gas reside in the magma, hence the gas content is defined by its volume fraction $\chi = V_g/(V_g + V_m)$; porosity as $\phi = (V_g + V_m)/(V_g + V_m + V_c)$. We can find that the volume ratios could be expressed as

$$\frac{V_g}{V_m} = \frac{\chi}{1-\chi}, \quad \frac{V_g}{V_c} = \frac{\phi}{1-\phi}\chi, \quad \frac{V_m}{V_c} = \frac{\phi}{1-\phi}(1-\chi)$$

Mass conservation of the volatiles is

$$c_o(\rho_g V_g + \rho_{crystal} V_c + \rho_m V_m) = \rho_g V_g + c\rho_m V_m + c_{crystal}\rho_{crystal} V_c$$

which leads to the gas volume fraction as a function of crystalinity/porosity $\chi = \frac{(c_o - c)\left(1 + \frac{\rho_c}{\rho_m}\frac{1-\phi}{\phi}\right)}{c_o - c + \frac{\rho_g}{\rho_m}(1-c_o)}$ As shown in Figure A1, for magma with 5wt% pre-exsolution volatile concentration, in-situ crystalization of 70vol% crystals (i.e., $\phi = 0.3$) could increase the gas volume fraction from 10% to 30% at a depth of 3.5km (assuming that pressure is the primary driver for gas exsolution), hence our choice of $\chi = 0.3, \chi_c = 0.1$ in the main text. We also find that on the scale of 1MPa pressure perturbation (i.e., corresponding to 0.04km depth change), the exsolved gas volume fraction could alter by 1vol%.

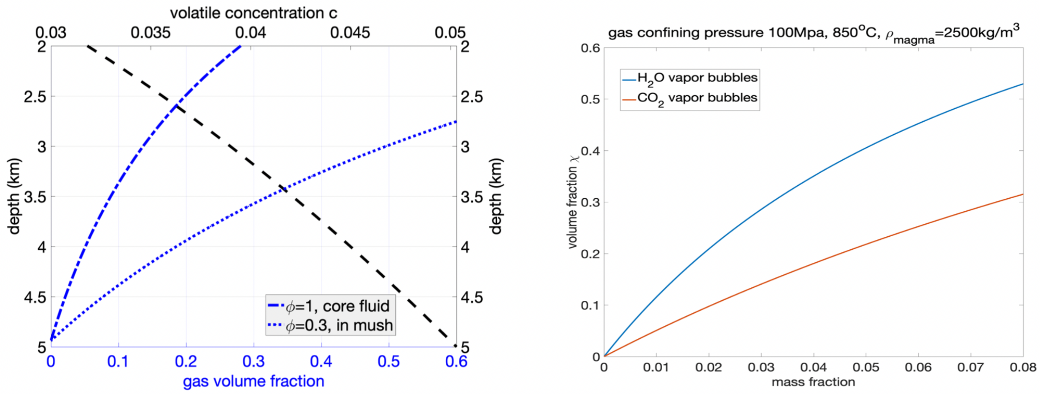

(a) (b)

Figure A1. (a) Estimation of volatile (H2O) concentration in magma and exsolved gas volume fraction as functions of depth for different crystalinity. The system contains 5% dissolved volatile prior to gas exsolution and crystalization. Black dash line (top x axis) shows the concentration of dissolved volatile in magma decreasing with depth; blue lines show increase of exsolved gas volume fraction in magma as function of depth. The case of $\phi = 1$ corresponds to core magma with no crystals; the case for $\phi = 0.3$ corresponds to pore magma in crystal mush. We note from the figure that on a scale of 1MPa pressure fluctuation (the observed value from our finding) corresponds to depth change of 0.04km, which could cause gas volume fraction to vary on the scale of 1%. (b) Gas volume fraction as functions of gas mass fraction. The curves are calculated according to ideal gas law for two different molecular weight (CO2 and water) under confining pressure 100MPa and temperature of 850^oC. Petrological evidence suggests gas mass fraction of 0-8wt% in magmatic reservoirs, which according to the curves correspond to 0-30 vol% for CO_2 and 0-55vol% for H_2O.

The aspect of gas is factored in the model via its effect on the bulk modulus and thermal expansion coefficient of the magma in the core and/or the pores. Assuming ideal gas, the isothermal bulk modulus for gas is $K_g = \rho_g \frac{dP_g}{d\rho_g} = P_g$. We obtain the effective bulk modulus of the magma-gas ensemble: deforming (e.g. compressing) the whole material, the gas and magma both deform, but the pressure change in gas, magma, and the whole ensemble is the same ΔP. The total volume change is $\Delta V = \Delta V_m + \Delta V_g$, and fluid/gas pressure change is $\Delta P = -K_m \frac{\Delta V_m}{V_m} = -K_g \frac{\Delta V_g}{V_g}$. This pressure change can also be expressed by the effective bulk modulus $\Delta P = -K_{eff} \frac{\Delta V_m + \Delta V_g}{V_m + V_g}$. These two relations lead to the effective bulk modulus

$$K_{eff} = \frac{K_m K_g}{(1-\phi)K_g + \phi K_m}$$

Similarly, thermal expansion coefficient $\frac{\Delta V_g}{V_g} = \beta_g \Delta T$, hence $\beta_{eff} = \phi\beta_f + (1-\phi)\beta_m$.

A5 Other values

The dimensionless values are assumed based on existing models and observations. The competition between thermal and poroelastic diffusion is reflected by the ratio of their respective diffusivity κ_T/c. There is no available thermal diffusivity measurements for crystal mush, and here we assume that κ_T is of similar value of the thermal diffusivity for magma $\kappa_T \sim 8 \times 10^{-7} m^2/s$ (which is of similar order of magnitude for the thermal diffusivity of rocks), following previous studies by assuming permeability $\kappa \in$

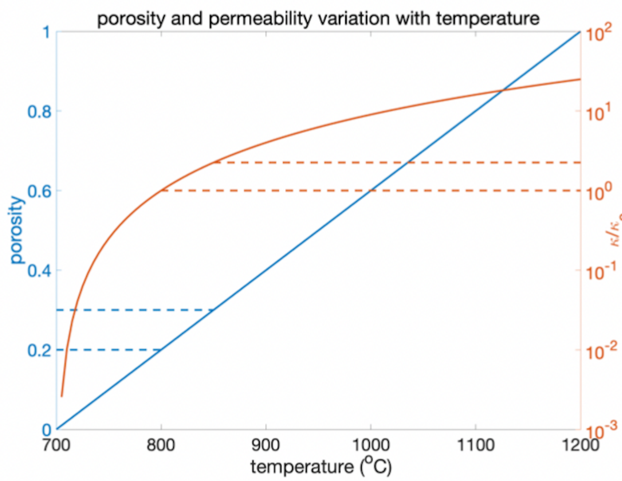

Figure A2. Porosity ϕ (left axis) and permeability κ (right axis) variation with temperature. The porosity is assumed linear with temperature between liquidus (1200^oC) and solidus (700^oC), and permeability $\kappa/\kappa_o = (\phi/\phi_o)^2$. broken lines indicate the porosity and permeability for the range of temperature (800-850^oC) considered in the current study.

$[10^{-11}, 10^{-8}]m^2$, magma viscocity $\eta_m = 100Pa.s$ and elastic moduli of the order of GPa, we find that the poroelastic diffusivity $c_{poro} \in [3{\times}10^{-5}, 0.2]m^2/s$, leading to $\frac{c_{thermal}}{c_{poro}} \in [4 \times 10^{-6}, 3 \times 10^{-2}]$.

Second, the competition between poroelastic diffusion and relaxation can be reflected by the definition of the diffusion-relaxation length $[l] \equiv \sqrt{\tau_r c}$ and the ratio $r_o/[l]$. By the definition of $[l]$, it is the length over which poroelastic diffusion and viscoelastic relaxation occur with the same speed; hence $r_o/[l] > 1$ means faster viscoelastic relaxation over the thickness of the mush shell, $r_o/[l] < 1$ indicates faster poroelastic diffusion over the thickness of the mush, and $r_o/[l] = 1$ indicates that the two processes occur at the same rate over the mush shell. Based on the range of parameters we find that $[l]$ could have a large range, given the uncertainty of permeability, magma viscosity, and relaxation time. According to previous studies, the relaxation time $\tau_r \in [4mon, 30year]$ (Segall, 2016; Liao et al., 2021). With the range for poroelastic diffusivity shown above, we find that $[l] \in [18m, 14km]$, hence for magma chamber on from 500m- 2km, $r_o/[l]$ range from 0.03 to 100. In most of the examples we show below, we consider $r_o/[l] = 1$.